Journal of Materials Chemistry A

COMMUNICATION

View Article Online
View Journal | View Issue

Cite this: J. Mater. Chem. A, 2015, 3, 15008

Received 6th May 2015
Accepted 16th June 2015

DOI: 10.1039/c5ta03312h

www.rsc.org/MaterialsA

Nanomeshes of highly crystalline nitrogen-doped carbon encapsulated Fe/Fe_3C electrodes as ultrafast and stable anodes for Li-ion batteries†

Jinqiu Zhou, Tao Qian,* Tingzhou Yang, Mengfan Wang, Jun Guo and Chenglin Yan*

Fe/Fe_3C homogeneously dispersed in 2D porous nitrogen-doped graphitic carbon nanomeshes (N-Fe/Fe_3C@C nanomeshes) was prepared by a novel template-free method using the polypyrrole–Fe (PPy–Fe) coordination complex as a precursor. The designed architecture is beneficial to electron transport and accommodation of the strains of Li insertion/extraction. As an anode material for Li-ion batteries, the as-prepared composite exhibits a reversible capacity of 1316 mA h g^{-1} (normalized to the mass of Fe/Fe_3C in the composite) with extremely excellent cycling performance at high rate (nearly 100% capacity retention after 500 cycles) and good rate capability. The synthesis approach presents a promising route for a large-scale production of N-Fe/Fe_3C@C nanomesh composites as an extremely durable high-rate anode material for Li-ion batteries.

Introduction

Carbon nanomeshes,[1–4] emerged as a new type of nanostructure, have attracted great interest because of their promising applications in a wide range of areas,[5–7] in view of their fantastic architecture and tunable properties. In the field of lithium ion batteries, amorphous carbon coating is usually utilized to prevent electrode materials from collapse; however, the amorphous structure possesses the drawback of low electric conductivity as compared to its crystalline counterparts, resulting in the deterioration of capacity retention and low rate capability. In contrast, highly crystalline carbon nanomeshes exhibit high electrical conductivity that is beneficial for enhancing rate capability and strain accommodation for lithium ion batteries (LIBs). A common synthetic strategy for the fabrication of nanomesh structures employs sacrificial templates. For example, thermally stable NaCl particles were used as a template to synthesize the graphite nanomesh by He *et al.*;[7] porosity control over nitrogen-doped carbon nanosheets with uniform and tunable mesopores was achieved by employing an appropriate graphene/silica nanosheet template by Wei *et al.*;[6] well-ordered thin-film nanopore arrays were formed using a block-copolymer template by Jung *et al.*[8] However, template methods are usually time consuming and costly because of the need for the synthesis of templates and multi-step templating processes. Therefore, developing facile, scalable template-free approaches for the rational synthesis of nanomesh structures is highly desirable.[9]

On the basis of the available lithium storage mechanisms, Fe nanoparticles are inert to react with Li^+ and contribute nothing to electrochemical Li storage and Fe_3C can store only 1/6 Li per unit (~26 mA h g^{-1}). This does not mean that Fe/Fe_3C nanoparticles contribute nothing to lithium storage. Actually, Fe/Fe_3C nanoparticles might serve as electrocatalysts for the reversible conversion of some components of solid electrolyte interface films, and provide extra capacity to the active materials.[10–12] As a result, Fe_3C nanomaterials as anodes for LIBs could show desirable properties based on conversion mechanics with the advantages of high capacity, non-toxicity, high abundance, high corrosion resistance, and low processing cost. However, as far as we know, Fe_3C-based nanomaterials are generally used as high-performance magnets and catalysts,[13–16] and carbides have scarcely been touched as LIB anode materials due to two troublesome obstacles.[17,18] One is the volume expansion/contraction during repeated cycling processes. Another is that the low conductivity of pristine carbides[19] also induces performance degradation, particularly when charging and discharging at high current rates. In order to circumvent the above intractable problems, strategies have been proposed to enhance the structural stability of electrode materials.[6] It has been widely demonstrated that this problem can be partly solved in nanostructured electrode materials with various morphologies, including nanoparticles, nanosheets, nanowires, nanorods, nanotubes, and other hollow

College of Physics, Optoelectronics and Energy & Collaborative Innovation Center of Suzhou Nano Science and Technology, Soochow University, No. 1 Shizi Street, Suzhou 215006, China. E-mail: c.yan@suda.edu.cn; tqian@suda.edu.cn

† Electronic supplementary information (ESI) available. See DOI: 10.1039/c5ta03312h

nanostructures.[20–23] Another approach is to integrate a carbonaceous matrix into active materials to form hybrid nanostructures. Typically, the carbon components in the hybrid materials are anticipated to serve dual functions: as conducting additives to promote electron transport in poorly conductive materials and as elastic buffer supports to enhance the stability of electrodes.[6,24–31]

For upcoming large-scale applications, the notion of material sustainability produced by materials made through eco-efficient processes such as renewable organic methods is crucial. Great attention has been paid to conduct research on fabricating electrode materials through organic methods.[32–36] Polypyrrole (PPy), as a kind of source for nitrogen doping,[37–39] is an intrinsically organic polymer material with high conductivity, storage ability, redox and capacitive current and good thermal and environmental stability.[40–44] Additionally, certain nitrogen doping is an appropriate method for strengthening the surface wettability of materials, capacity, and electrical conductivity while maintaining superb cyclability.[45] Herein, a facile, ingenious and template-free synthesis strategy was attempted to produce N-doped carbon nanomesh encapsulated Fe/Fe_3C (N-Fe/Fe_3C@C). The fabrication process involves the novel synthesis of the PPy–Fe coordination complex and carbonization of the prepared precursor. It is found that the constructed unique 2D architecture not only avoids the direct exposure of encapsulated Fe/Fe_3C to the electrolyte to preserve the structural and interfacial stabilization of Fe/Fe_3C, but also accommodates the mechanical stress induced by the volume change of the embedded Fe/Fe_3C nanoparticles as well as inhibits the aggregation of Fe/Fe_3C, which thus maintains the structural and electrical integrity. As a result, the prepared anode exhibits very high reversible specific capacity, ultrafast rate performance and especially high cycling stability. Notably, the starting materials and the synthetic processes are both viable for large-scale production, making this approach particularly attractive for practical applications.

Experimental

Materials preparation

PPy spheres were synthesized according to a reported method.[42] 0.35 g of $FeCl_2$ and 20.0 mL of H_2O_2 were added to the deep dark solution of PPy spheres. After continuously stirring overnight, the deep dark solution became bright yellow and transparent. The solution was dried under vacuum to obtain a dark yellow product. After that, the as-prepared materials were heated at 900 °C for 2 h in a tube furnace under flowing Ar (200 sccm) and H_2 (40 sccm) atmospheres to obtain N-Fe/Fe_3C@C nanomeshes. To obtain N-doped carbon nanomeshes, the N-Fe/Fe_3C@C was leached in 6 M HNO_3 solutions for 24 h and then washed with deionized water three times.

Physical characterization

Elemental analysis was carried out on an X-ray photoelectron spectrometer (Kratos Axis Ultra Dld, Japan). Fourier-transform infrared (FT-IR) spectra were recorded on a Nicolet is 50 spectrometer (Themo Fisher Scientific, America). A UV-Vis-NIR Spectrophotometer (SHIMADZU company, Japan) was used to perform UV-Vis-NIR spectra analysis. The morphology was observed with a field emission scanning electron microscope (FESEM, SU8010, Japan), and a field emission transmission electron microscope (FETEM, FEI Tecnai G2 F20 S-TWIN TMP, Hongkong). X-ray diffraction (XRD) measurements were performed on a Rigaku D/max-2000PC diffractometer with Cu KR radiation. Thermogravimetric analysis (TGA) was performed with a SDT 2960 (TA Instruments) up to 800 °C at a heating rate of 10 °C min^{-1} in air. Raman spectra were recorded on a HR800 (HORIBA Jobin Yvon) Raman spectrometer. An inductively Coupled Plasma (ICP) emission spectrometer (OPTIMA 8000) was used to determine the content of the Fe element.

Electrochemical evaluation

Electrodes were prepared by mixing the as-prepared powder (70 wt%), carbon black (20 wt%) and polytetrafluoroethylene binder (PTFE, 10 wt%), casted onto a piece of nickel foam with a mass loading of ~0.8 mg cm^{-2}. Electrode sheets were dried under vacuum at 60 °C for 24 h. Coin cells (CR2025) were fabricated with fresh lithium foil as the counter electrode, 1 mol L^{-1} $LiPF_6$ dissolved in a mixture of ethylene carbonate (EC), ethyl methyl carbonate (EMC) and diethyl carbonate (DEC) (4 : 3 : 3 vol%) as the electrolyte, and Celgard 2400 as the separator. The assembly of the cell was conducted in an Ar-filled glovebox followed by an overnight aging treatment before the test. Cyclic voltammetry (CV) measurements were conducted at 0.1 mV s^{-1} within the range of 0.0–3.0 V on a CHI 660E electrochemical workstation. Electrochemical impedance spectroscopy (EIS) was also performed on this electrochemical workstation over the frequency range of 100 kHz to 0.01 Hz. The cycle life and rate capability of the cells were tested within a voltage window of 0.0–3.0 V (*vs.* Li^+/Li) by using a battery testing system (LAND CT 2001A, Wuhan, China) at room temperature.

Results and discussion

The fabrication process for the N-Fe/Fe_3C@C hybrid nanomeshes principally consists of two steps as shown in Fig. 1. The first step involves the synthesis of the PPy–Fe coordination complex. After the addition of extra $FeCl_2$ and H_2O_2, the color of the solution transformed from deep dark to bright yellow and finally to transparent (Fig. 2A). In the second step, the PPy–Fe complex was calcined at 900 °C for 2 h under flowing Ar and H_2 atmospheres, thus yielding discrete and homogeneous N–carbon-encapsulated Fe/Fe_3C uniformly dispersed in graphitic carbon nanomeshes. To explore the formation mechanism of the PPy–Fe coordination complex, the structural changes in the PPy–Fe coordination complex were investigated by comparing the XPS spectra (Fig. 2B). In the survey region of 0 to 800 eV, it is evident that C, O, and N elements all exist in two samples while the Fe element appears in the PPy–Fe only. The high-resolution C1s (Fig. S1A†) is clearly divided into four components at 284.7, 285.3, 286.5 and 288.3 eV corresponding to C–C, C–N, C=N and C=O.[46] The intensity of C=N is weakened, while the intensity

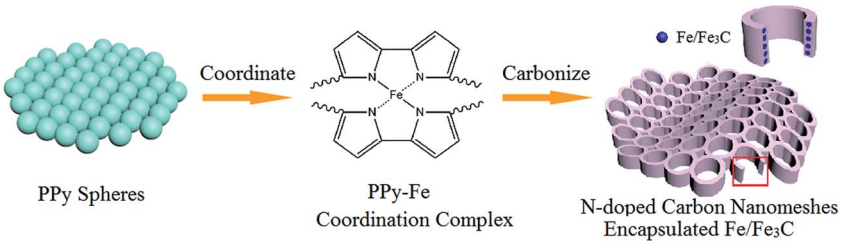

Fig. 1 Schematic representation of the synthesis of N-Fe/Fe_3C@C nanomeshes.

of C–N is enhanced after coordinating, which implies the coordination reaction of Fe ions and N atoms. Comparing the N1s XPS spectrum (Fig. S1B†), the appearance of the –NH^+– (401.5 eV)[46] peak indicates that the N atoms coordinated with Fe ions, whereas the H ions partly remained. Additionally, the Fe2p peak appeared at 709.8 eV further justifies the successful synthesis of the PPy–Fe coordination complex (Fig. S1C†). FT-IR analysis of the pure PPy and PPy–Fe coordination complex was performed to recognize the change of the interactions within the complex after the formation of the complex (Fig. 2C). The stretching positions of the C=C backbone (at 1549 cm^{-1}), the C–C ring (at 1445 cm^{-1}) and C–N (at 1380 cm^{-1}) arising from PPy were further confirmed by the emergence of the pyrrole ring vibration located at 964 cm^{-1}.[33] The presence of an imine-like nitrogen (C=N–, at 2200 cm^{-1})[46] and a C=O structure (at 1700 cm^{-1})[47] is consistent with the structure of overoxidized polypyrrole. After the coordination, peaks at 1380 cm^{-1} (C–N stretching vibration)[35] and 750 cm^{-1} (C–O stretching vibration in epoxide) are enhanced and a new peak at about 3050 cm^{-1} (free hydrogen atoms) appears, indicating the occurrence of the coordination reaction. The disappearance of the peak at 2200 cm^{-1} indicates that the imine-like nitrogen ring changes to pyrrole-like N through the formation of a Fe–N bond, which was the evidence of the extrapolation from the XPS spectra.

The morphologies of N-Fe/Fe_3C@C nanomeshes were examined by SEM and TEM, which are shown in Fig. 3. The low-magnification image in Fig. 3A shows a thin wrinkled "paper-like" structure with a thickness of about 150 nm. Fig. 3B presents a typical low-magnification TEM image of Fe/Fe_3C@C nanosheets, which demonstrates that these micrometer-sized nanosheets appear as a foam-like porous graphitic structure hybridized with Fe/Fe_3C particles, as shown in Fig. 3C. High-magnification TEM images (Fig. 3D) of N-Fe/Fe_3C@C nanomeshes clearly reveal that the carbon meshes present a very

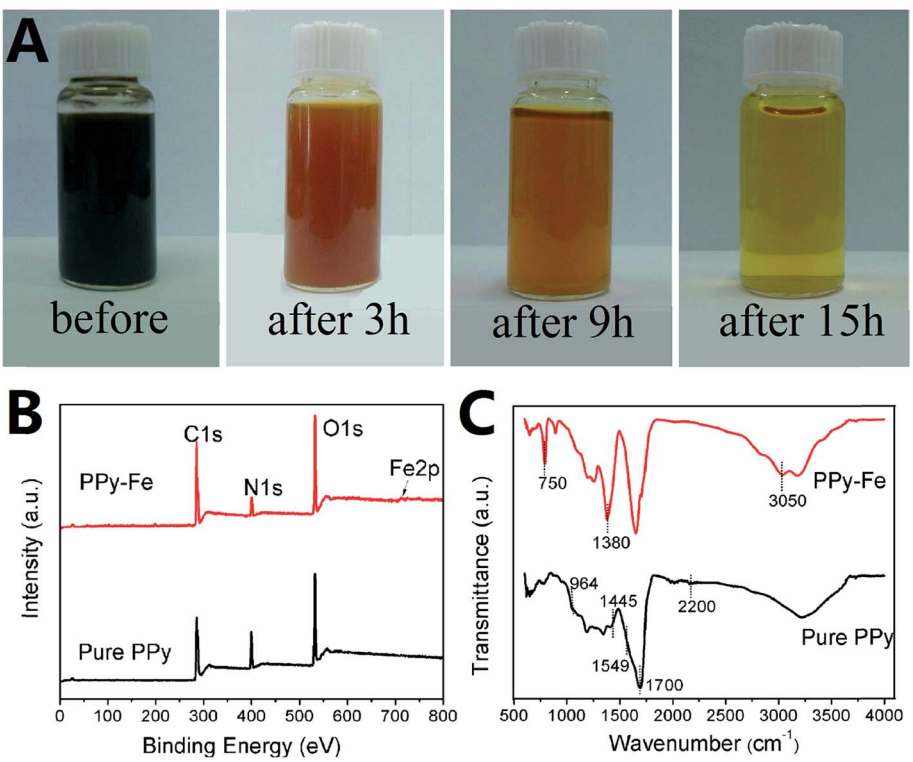

Fig. 2 (A) The color of the obtained solution (before and after 3 h, 9 h, 15 h from left to right) (B) the full XPS spectra (C) FT-IR spectra of the pure PPy and PPy–Fe coordination complex.

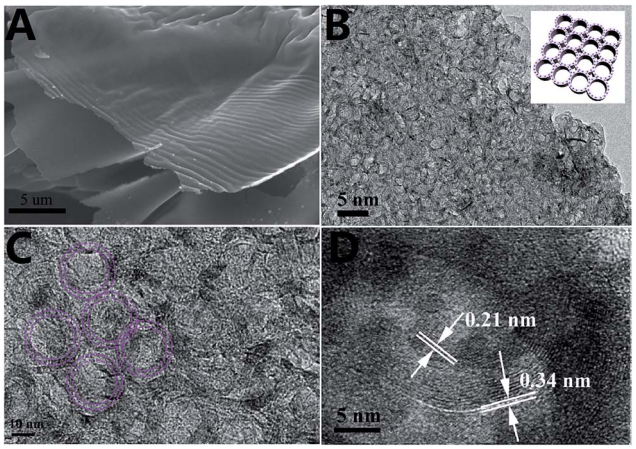

Fig. 3 (A) SEM and (B–D) TEM images of the nitrogen doped Fe/Fe_3C@C nanomeshes. The inset in (B) is a top-view schematic of the nitrogen doped Fe/Fe_3C@C nanomeshes.

high degree of graphitization showing lattice fringe with a *d*-spacing of 0.34 nm which is in good agreement with that of the (002) planes of graphite.[6,48] A well-defined crystalline lattice spacing of 0.21 nm was observed in Fig. 3D, which is consistent with the (211) diffraction peak of Fe_3C[12] and the (110) plane of metallic Fe.[49] As shown in Fig. 4A, the diffraction peak at 26.5° corresponds to the (002) plane of graphitic carbon, while the peaks located at 44.8° and 65.1° are attributed to the *in situ* formation of Fe (JCPDS, no. 89-7194). The rest of diffraction peaks are characteristics of the crystalline planes of Fe_3C species (JCPDS, no. 89-2867).[10–13] For further supporting the existence of Fe_3C, the selected area electron diffraction (SAED) pattern[50–52] of N-Fe/Fe_3C@C nanomeshes is shown in the inset of Fig. 4A. The diffraction peaks indicated by white arrows are the characteristic peaks (200), (040) and (141) of Fe_3C with lattice spacings differing from Fe, which provides powerful evidence supporting the existence of Fe_3C. Additionally, the broad peak around $2\theta = 22°$ is associated with the planar aromatic rings of pyrrole,[53–55] further confirming the nitrogen-doped structure. XPS was carried out in the region of 0–1100 eV, as shown in Fig. 4B. The distinct peaks at 285 and 532 eV correspond to C1s and O1s, however, no Fe2p signal was observed.[6,56] The high-resolution C1s (Fig. S4A†) is clearly divided into four components at 284.7, 285.3, 286.6 and 288.7 eV corresponding to C–C, C–N, and C=N, C=O, respectively. Comparing with the C1s spectrum of the PPy–Fe coordination complex, it is evident that the intensity of C=O is weakened and the intensity of C–C is enhanced after carbonization. As shown in Fig. S4B,† a trivial N1s signal was observed with a share of nitrogen atoms (~3.53 wt%, Fig. 4C). The Raman spectrum is shown in Fig. 4D wherein the G band occurs at 1596 cm^{-1}(G means "graphitic") and the D band occurs at 1340 cm^{-1} (D means "disorder").[57] The value of I_D/I_G reflecting the degree of crystallinity of carbon structures[6] is determined to be ~1. It is well accepted that the D band may be activated or

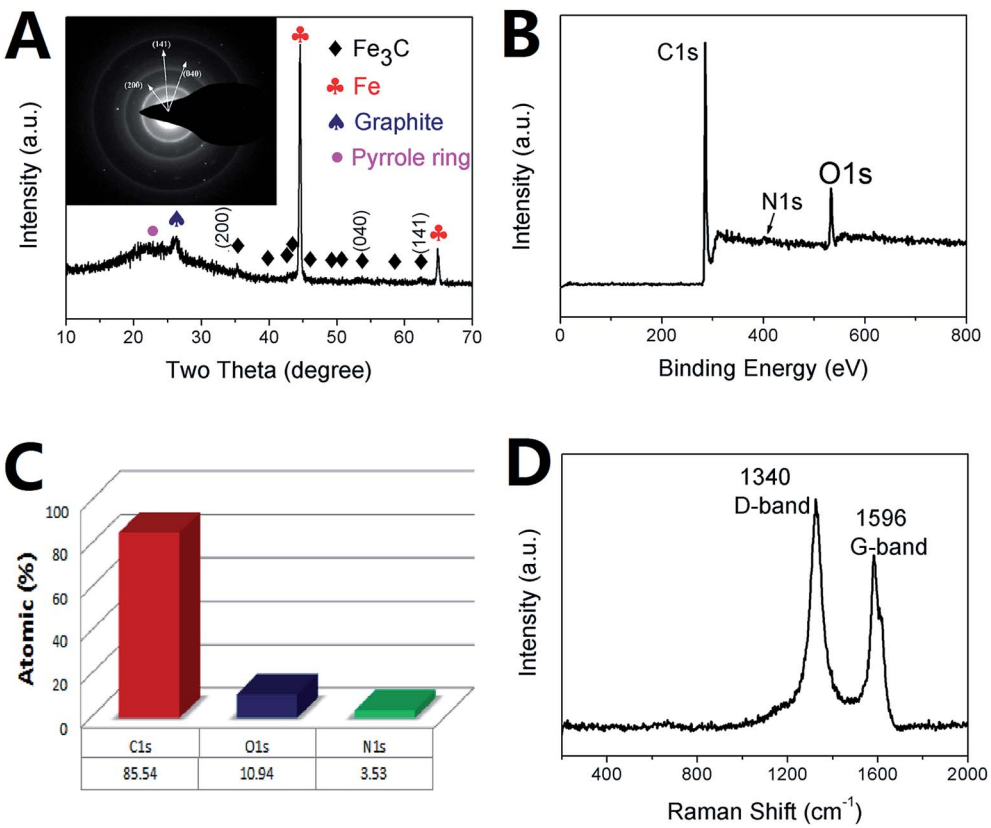

Fig. 4 (A) XRD pattern, (B) full XPS spectrum, (C) the element content of the N-Fe/Fe_3C@C nanomeshes obtained from XPS measurements and (D) Raman spectrum of the N-Fe/Fe_3C@C nanomeshes. The inset of (A) is the SAED pattern of N-Fe/Fe_3C@C nanomeshes.

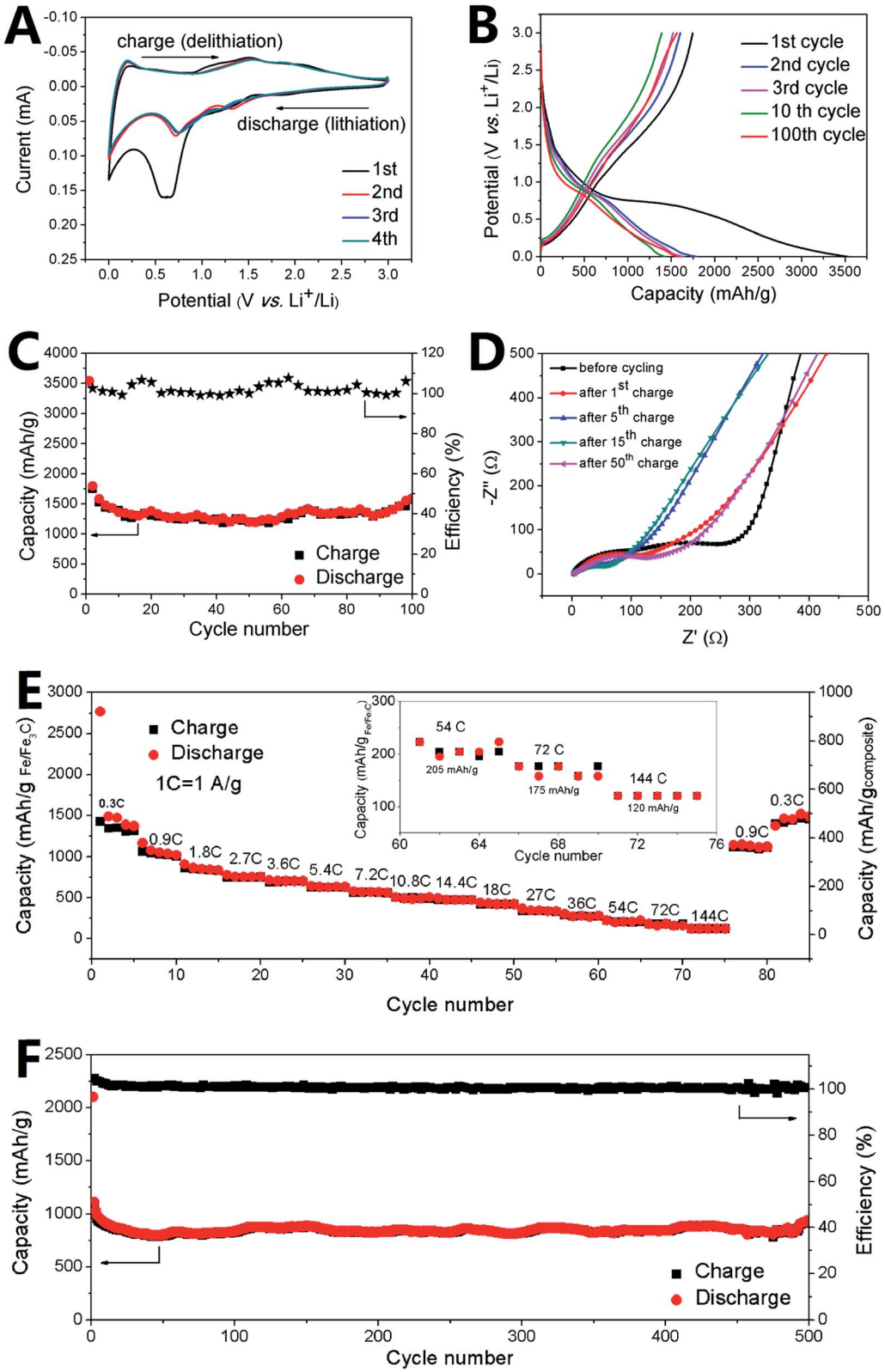

Fig. 5 (A) Representative CV curves of an electrode based on N-Fe/Fe_3C@C nanomeshes obtained in a voltage range of 0.0 to 3.0 V (*vs.* Li^+/Li) and a potential scan rate of 0.1 mV s^{-1}. (B) Voltage profiles plotted for the first, second, third, 10th, 100th cycles at a current density of 300 mA g^{-1}. (C) Charge/discharge capacities and the efficiency of the prepared coin cell at a current density of 300 mA g^{-1}. (D) Nyquist plots at fresh coin cells over the frequency range of 100 kHz to 0.01 Hz. (E) Charge/discharge capacity at various rates for 90 cycles, and the inset shows the rate capability at higher current rates. (F) Charge/discharge capacities and the efficiency of the electrode at a high current density of 3600 mA g^{-1} for 500 cycles. All the specific capacities and current densities are calculated based on the mass of Fe/Fe_3C in the composite.

enhanced by in-plane substitutional heteroatoms or introduction of defects. N doping is very effective in introducing defects into the structure, which is consistent with a large body of literature. TGA (seen in Fig. S4D†), carried out in air at a heating rate of 10 °C min^{-1} from room temperature to 800 °C, was used to determine the mass of Fe/Fe_3C in the composite. According to the remaining weight of Fe_2O_3 (45.6 wt%) due to the oxidation reaction of Fe/Fe_3C, the original fraction of Fe/Fe_3C is calculated to be ~34.2 wt%. Additionally, an ICP Emission Spectrometer was used to further determine the Fe content of N-Fe/Fe_3C@C nonomeshes. The result (~34 wt%) is in accordance with that of TGA.

CV provides more details for the electrode redox processes during the electrochemical reaction. Fig. 5A shows the first four CV curves of the N-Fe/Fe_3C@C nonomesh electrodes between 0.0 and 3.0 V at a scan rate of 0.1 mV s^{-1}. It is clear that the CV curve of the first cycle is somewhat different from those of the subsequent cycles. A well-defined peak is observed ~0.5 V (*vs.* Li^+/Li) while the big slope corresponds to Li^+ insertion into carbon. However, the peak intensity drops from the second cycle, arising from irreversible side reactions on the electrode surfaces and interfaces mainly due to solid electrolyte interface (SEI) formation. The electrode exhibits obvious redox peaks and different potential ranges for lithium storage. The distinct peaks appear at 0.7 V and 1.4 V due to the polarization along with cycling during discharge and at 1.6 and 2.0 V during charge in the subsequent cycling. It is noteworthy that, after the first cycle, the voltage current curves almost overlapped, which is consistent with the outstanding cycling stability of the material, indicating that a stable SEI film formed in the first cycle can safeguard the structural integrity of the N-Fe/Fe_3C@C nanomesh composite during subsequent charge–discharge cycles, thus leading to the stable and superior reversibility of the sample.[6,15,33] Fe/Fe_3C nanoparticles play an indispensable role here and work within a novel mechanism, which can be evidently justified by the fact that the CV profile of N-Fe/Fe_3C@C is different from that of N-doped carbon nanomesh electrodes (Fig. S5†). Besides a similar peak in the first cycle for the SEI formation, no obvious reduction and oxidation peaks were observed in Fig. S5† and the area in the subsequent cycles was much lower than that of N-Fe/Fe_3C@C electrode.[15] Fig. 5B shows representative discharge/charge voltage profiles at a current density of 300 mA g^{-1} between 0.0 and 3.0 V, which delivers a very high lithium storage capacity of 3539 mA h g^{-1} during the initial discharge process, and the Coulombic Efficiency in the initial cycle is 50% and increases to nearly 100% during the subsequent cycles. It should be emphasized that no obvious change in both charge and discharge profiles is observed even after 100 cycles, indicating the extraordinarily stable performance of the nanomesh electrodes. To highlight the superiority of the unique N-Fe/Fe_3C@C nanomeshes for lithium storage materials, we tested the cycle performance of the electrode at a current density of 300 mA g^{-1} between 0.0 and 3.0 V *vs.* Li^+/Li (Fig. 5C). Apparently, the reversible capacity reaches 1316 mA h g^{-1} and demonstrates excellent cyclic retention. EIS was conducted at frequencies from 100 kHz to 0.01 Hz. Fig. 5D shows the EIS profiles of the as-prepared coin cell at different states: before cycling and after the 1^{st}, 5^{th}, 15^{th} and 50^{th} charging process. The R_{CT} (charge transfer resistance, approximate to the diameter of the semicircle) obviously reduces after the 1^{st}, 5^{th}, and 15^{th} cycle due to the building of Li-ion transport channels and then increases in the following cycles due to the polarization of the electrode.[58]

In addition to its superior stable performance, the N-Fe/Fe_3C@C nanomesh electrode also shows outstanding rate performance (Fig. 5E). To improve the rate capability of electrodes for LIBs, in our work, highly crystalline carbon nanomeshes rather than amorphous carbon structures were utilized for fast electron transport. As shown in Fig. 5E, the capacity only decreases from 1312, 1021, 836, 747, 696, 626, 564, 492, 474, 418, 334, 279, 205, 175 to 117 mA h g^{-1} when the current density increases in the order of 0.3C, 0.9C, 1.8C, 2.7C, 3.6C, 5.4C, 7.2C, 10.8C, 14.4C, 18C, 27C, 36C, 54C, 72C, and 144C (1C = 1 A g^{-1}). Surprisingly, even at an ultrahigh charge/discharge rate of 144C, it can still deliver a reversible capacity of 120 mA h g^{-1}. Moreover, when the current rate is finally returned to its initial current density of 0.9C and 0.3C after a total of 80 cycles, a capacity of 1114 and 1455 mA h g^{-1} respectively is still recoverable without any losses. The durability of this anode working at a higher rate (Fig. 5F) was investigated at a current density of 3600 mA g^{-1} for 500 cycles with a reversible capacity of 819 mA h g^{-1}, further demonstrating the extraordinary superior cycling stability of this structure even at ultrahigh charge/discharge rates.

Conclusions

In summary, to achieve ultrafast and stable anodes for lithium ion batteries, a new type of nitrogen doped Fe/Fe_3C@C nanomesh composite was fabricated by means of a template-free organic coordination complex method. The prepared electrodes deliver a high capacity of ~1316 mA h g^{-1} and an ultrafast charge/discharge rate of 144C, as well as nearly 100% capacity retention after 500 cycles. Our reported novel and high-yield strategy using the organic coordination complex as *in situ* doping resources can be extended to build a variety of other interesting materials for stable and ultrafast LIBs.

Acknowledgements

We acknowledge the support from the "Thousand Talents Program", the Natural Science Foundation of Jiangsu Province of China (no. BK20140315), the National Natural Science Foundation of China (no. 51402202), the National Basic Research Program of China (no. 2015CB358600), Jiangsu Shuangchuang Plan, and the Priority Academic Program Development of Jiangsu Higher Education Institutions (PAPD).

Notes and references

1 J. W. Bai, X. Zhong, S. Jiang, Y. Huang and X. F. Duan, *Nat. Nanotechnol.*, 2010, **5**, 190.
2 S. Berner, M. Corso, R. Widmer, O. Groening, R. Laskowski, P. Blaha, K. Schwarz, A. Goriachko, H. Over, S. Gsell, M. Schreck, H. Sachdev, T. Greber and J. Osterwalder, *Angew. Chem., Int. Ed.*, 2007, **46**, 5115.

3 H. S. Ahin and S. Ciraci, *Phys. Rev. B: Condens. Matter Mater. Phys.*, 2011, **84**, 035452.
4 U. Schlickum, R. Decker, F. Klappenberger, G. Zoppellaro, S. Klyatskaya, M. Ruben, I. Silanes, A. Arnau, K. Kern, H. Brune and J. V. Barth, *Nano Lett.*, 2007, **7**, 3813.
5 H. P. Zhao, C. L. Wang, R. Vellacheri, M. Zhou, Y. Xu, Q. Fu, M. H. Wu, F. Grote and Y. Lei, *Adv. Mater.*, 2014, **26**, 7654.
6 W. Wei, H. W. Liang, K. Parvez, X. D. Zhuang, X. L. Feng and K. Mullen, *Angew. Chem., Int. Ed.*, 2014, **53**, 1570.
7 C. N. He, S. Wu, N. Q. Zhao, C. S. Shi, E. Z. Liu and J. J. Li, *ACS Nano*, 2013, **7**, 4459.
8 Y. S. Jung and C. A. Ross, *Small*, 2009, **5**, 1654.
9 A. Q. Pan, H. B. Wu, L. Yu and X. W. Lou, *Angew. Chem., Int. Ed.*, 2013, **125**, 2282.
10 L. W. Su, Y. R. Zhong and Z. Zhou, *J. Mater. Chem. A*, 2013, **1**, 15158.
11 L. W. Su, Z. Zhou and P. W. Shen, *J. Phys. Chem. C*, 2012, **116**, 23974.
12 L. W. Su, Z. Zhou, X. Qin, Q. W. Tang, D. H. Wu and P. W. Shen, *Nano Energy*, 2013, **2**, 276.
13 Y. Hou, T. Z. Huang, Z. H. Wen, S. Mao, S. M. Cui and J. H. Chen, *Adv. Energy Mater.*, 2014, **4**, 1400337.
14 J. S. Lee, G. S. Park, S. T. Kim, M. L. Liu and J. Cho, *Angew. Chem., Int. Ed.*, 2013, **125**, 1060.
15 Z. H. Wen, S. Q. Ci, F. Zhang, X. L. Feng, S. M. Cui, S. Mao, S. L. Luo, Z. He and J. H. Chen, *Adv. Mater.*, 2012, **24**, 1399.
16 Y. Hu, J. O. Jensen, W. Zhang, L. N. Cleemann, W. Xing, N. J. Bjerrum and Q. F. Li, *Angew. Chem., Int. Ed.*, 2014, **53**, 3675.
17 M. Naguib, J. Come, B. Dyatkin, V. Presser, P. L. Taberna, P. Simon, M. W. Barsoum and Y. Gogotsi, *Electrochem. Commun.*, 2012, **16**, 61.
18 L. W. Su, Z. Zhou and P. W. Shen, *Electrochim. Acta*, 2013, **87**, 180.
19 K. Ichikawa and M. Achikita, *Mater. Trans.*, 1993, **16**, 718.
20 Y. G. Guo, J. S. Hu and L. J. Wan, *Adv. Mater.*, 2008, **20**, 2878.
21 N. Kang, J. H. Park, J. Choi, J. Jin, J. Chun, I. G. Jung, J. Jeong, J. G. Park, S. M. Lee and H. J. Kim, *Angew. Chem., Int. Ed.*, 2012, **51**, 6626.
22 Z. Y. Wang, L. Zhou and X. W. Lou, *Adv. Mater.*, 2012, **24**, 1903.
23 Z. M. Cui, L. Y. Jiang, W. G. Song and Y. G. Guo, *Chem. Mater.*, 2009, **21**, 1162.
24 S. B. Yang, X. L. Feng, S. Ivanovici and K. Mullen, *Angew. Chem., Int. Ed.*, 2010, **49**, 8408.
25 X. J. Zhu, Y. W. Zhu, S. Murali, M. D. Stoller and R. S. Ruoff, *ACS Nano*, 2011, **5**, 3333.
26 Z. C. Yang, J. G. Shen and L. A. Archer, *J. Mater. Chem.*, 2011, **21**, 11092.
27 T. Yoon, C. Chae, Y. K. Sun, X. Zhao, H. H. Kung and J. K. Lee, *J. Mater. Chem.*, 2011, **21**, 17325.
28 E. Kang, Y. S. Jung, A. S. Cavanagh, G. H. Kim, S. M. George, A. C. Dillon, J. K. Kim and J. Lee, *Adv. Funct. Mater.*, 2011, **21**, 2430.
29 J. S. Chen, Y. M. Zhang and X. W. Lou, *ACS Appl. Mater. Interfaces*, 2011, **3**, 3276.
30 J. Liu, Y. Zhou, F. Liu, C. Liu, J. Wang, Y. Pan and D. Xue, *RSC Adv.*, 2012, **2**, 2262.
31 Q. Qu, S. Yang and X. Feng, *Adv. Mater.*, 2011, **23**, 5574.
32 S. W. Wang, L. J. Wang, K. Zhang, Z. Q. Zhu, Z. L. Tao and J. Chen, *Nano Lett.*, 2013, **13**, 4404.
33 M. Armand, S. Grugeon, H. Vezin, S. Laruelle, P. Ribière, P. Poizot and J. M. Tarascon, *Nat. Mater.*, 2009, **8**, 120.
34 F. R. Brushett, J. T. Vaughey and A. N. Jansen, *Adv. Energy Mater.*, 2012, **2**, 1390.
35 Y. Mao, Q. Y. Kong, B. K. Guo, X. P. Fang, X. W. Guo, L. Shen, M. Armand, Z. X. Wang and L. Q. Chen, *Energy Environ. Sci.*, 2011, **4**, 3442.
36 Y. Mao, Q. Y. Kong, L. Shen, Z. X. Wang and L. Q. Chen, *J. Power Sources*, 2014, **248**, 343.
37 F. H. Du, B. Li, W. Fu, Y. J. Xiong, K. X. Wang and J. S. Chen, *Adv. Mater.*, 2014, **26**, 6145.
38 T. Qian, C. F. Yu, S. S. Wu and J. Shen, *Biosens. Bioelectron.*, 2013, **50**, 157.
39 T. Z. Yang, T. Qian, M. F. Wang, J. Liu, J. Q. Zhou, Z. Z. Sun, M. Z. Chen and C. L. Yan, *J. Mater. Chem. A*, 2015, **3**, 6291.
40 T. Qian, N. Xu, J. Q. Zhou, T. Z. Yang, X. J. Liu, X. W. Shen, J. Q. Liang and C. L. Yan, *J. Mater. Chem. A*, 2015, **3**, 488.
41 X. J. Liu, T. Qian, N. Xu, J. Q. Zhou, J. Guo and C. L. Yan, *Carbon*, 2015, **92**, 348.
42 T. Qian, S. S. Wu and J. Shen, *Chem. Commun.*, 2013, **49**, 4610.
43 T. Qian, X. Zhou, C. F. Yu, S. S. Wu and J. Shen, *J. Mater. Chem. A*, 2013, **1**, 15230.
44 C. Zhou, Y. W. Zhang, Y. Y. Li and J. P. Liu, *Nano Lett.*, 2013, **13**, 2078.
45 L. F. Chen, X. D. Zhang, H. W. Liang, M. G. Kong, Q. F. Guan and P. Chen, *ACS Nano*, 2012, **6**, 7092.
46 D. H. Nam, S. J. Lim, M. J. Kim and H. S. Kwon, *RSC Adv.*, 2013, **3**, 16102.
47 Y. F. Li and R. Y. Qian, *Electrochim. Acta*, 2000, **45**, 1727.
48 J. Qu, Y. X. Yin, Y. Q. Wang, Y. Yan, Y. G. Guo and W. G. Song, *ACS Appl. Mater. Interfaces*, 2013, **5**, 3932.
49 M. Q. Wang, W. H. Yang, H. H. Wang, C. Chen, Z. Y. Zhou and S. G. Sun, *ACS Catal.*, 2014, **4**, 3928.
50 M. M. Lu, W. Q. Cao, H. L. Shi, X. Y. Fang, J. Yang, Z. L. Hou, H. B. Jin, W. Z. Wang, J. Yuan and M. S. Cao, *J. Mater. Chem. A*, 2014, **2**, 10540.
51 B. Wen, X. X. Wang, W. Q. Cao, H. L. Shi, M. M. Lu, G. Wang, H. B. Jin, W. Z. Wang, J. Yuan and M. S. Cao, *Nanoscale*, 2014, **6**, 5754.
52 H. J. Yang, M. S. Cao, Y. Li, H. L. Shi, Z. L. Hou, X. Y. Fang, H. B. Jin, W. Z. Wang and J. Yuan, *Adv. Opt. Mater.*, 2014, **2**, 214.
53 X. F. Lu, D. M. Chao, J. Y. Chen, W. J. Zhang and Y. Wei, *Mater. Lett.*, 2006, **60**, 2851.
54 S. Y. Jing, S. X. Xing, L. X. Yu and C. Zhao, *Mater. Lett.*, 2007, **61**, 4528.
55 L. L. Qiu, S. C. Zhang, L. Zhang, M. M. Sun and W. K. Wang, *Electrochim. Acta*, 2010, **55**, 4632.
56 Y. Chen, B. H. Song, M. Li, L. Lu and J. M. Xue, *Adv. Funct. Mater.*, 2014, **24**, 319.
57 J. H. Kaufman and S. Metin, *Phys. Rev. B: Condens. Matter Mater. Phys.*, 1989, **39**, 13053.
58 Z. P. Song, Y. M. Qian, X. Z. Liu, T. Zhang, Y. B. Zhu, H. T. Yu, M. Otanibd and H. S. Zhou, *Energy Environ. Sci.*, 2014, **7**, 4077.

